Available online at www.sciencedirect.com
ScienceDirect
Journal of Structural Biology 155 (2006) 470–481
Journal of Structural Biology
www.elsevier.com/locate/yjsbi

Automated cryoEM data acquisition and analysis of 284742 particles of GroEL

Scott M. Stagg [a], Gabriel C. Lander [a], James Pulokas [a], Denis Fellmann [a], Anchi Cheng [a], Joel D. Quispe [a], Satya P. Mallick [a,b], Radomir M. Avila [a], Bridget Carragher [a], Clinton S. Potter [a,*]

[a] *The National Resource for Automated Molecular Microscopy, Department of Cell Biology, The Scripps Research Institute, La Jolla, CA 92037, USA*
[b] *Electrical and Computer Engineering, University of California, San Diego, USA*

Received 8 February 2006; received in revised form 7 April 2006; accepted 14 April 2006
Available online 22 May 2006

Abstract

One of the goals in developing our automated electron microscopy data acquisition system, Leginon, was to improve both the ease of use and the throughput of the process of acquiring low dose images of macromolecular specimens embedded in vitreous ice. In this article, we demonstrate the potential of the Leginon system for high-throughput data acquisition by describing an experiment in which we acquired images of more than 280 000 particles of GroEL in a single 25 h session at the microscope. We also demonstrate the potential for an automated pipeline for molecular microscopy by showing that these particles can be subjected to completely automated procedures to reconstruct a three-dimensional (3D) density map to a resolution better than 8 Å. In generating the 3D maps, we used a variety of metadata associated with the data acquisition and processing steps to sort and select the particles. These metadata provide a number of insights into factors that affect the quality of the acquired images and the resulting reconstructions. In particular, we show that the resolution of the reconstructed 3D density maps improves with decreasing ice thickness. These data provide a basis for assessing the capabilities of high-throughput macromolecular microscopy.
© 2006 Elsevier Inc. All rights reserved.

Keywords: TEM; Automation; Metadata; CryoEM; Database; Single particle reconstruction

1. Introduction

Cryo-electron microscopy (cryoEM) and single particle reconstruction (Frank, 2005) are becoming part of the standard armamentarium of structural techniques used for studying macromolecular assemblies. Single particle reconstruction relies on acquiring large numbers of images of the specimen of interest and using image analysis techniques to orient and classify the particles and reconstruct a three-dimensional electron density map. The resolution of the final model is dependent on a number of factors including the number of particles that contribute to the reconstructed volume. Practical experience (Gabashvili et al., 2000; Ludtke et al., 2004; Unwin, 2003) as well as theoretical estimates (Glaeser, 1999, 2004; Henderson, 1995) indicate that ~100 000 asymmetric subunits must be averaged together to produce a 3D map with a resolution below ~10 Å and ~1 000 000 subunits will be required to reach a resolution where it is possible to trace the protein chain. These numbers clearly indicate the necessity of automating the data acquisition and processing to the largest extent possible.

Over the past several years we have been developing an automated system, called Leginon, to acquire images from vitreous ice specimens (Carragher et al., 2000; Suloway et al., 2005). The system is designed to reproduce the decisions and actions of an experienced microscopist, including identifying suitable targets for imaging at a variety of scales, setting focus and astigmatism, checking

* Corresponding author. Fax: +1 858 784 9090.
E-mail address: cpotter@scripps.edu (C.S. Potter).

1047-8477/$ - see front matter © 2006 Elsevier Inc. All rights reserved.
doi:10.1016/j.jsb.2006.04.005

for specimen drift, and acquiring high-magnification images of the specimen under low dose conditions. An integral part of the Leginon system is a relational database (Fellmann et al., 2002) that keeps track of every image acquired to the CCD camera during the course of an experiment as well as all conditions used in acquiring the data.

It is often unclear what are the limiting factors in generating a high-resolution reconstruction. Are more particles needed? Was the specimen drifting too much? Is the CTF estimated poorly? Is the ice too thick? It can be extremely difficult if not impossible for the researcher to address these questions if the data were collected manually. Since Leginon logs information to a relational database for each image acquired, we are able to query the database for images with user-specified image parameters, e.g. we can query the database for images within a narrow range of ice thickness or drift, etc. The database thus becomes a powerful tool for sorting out what are the "best" data.

In this article, we demonstrate the potential of the Leginon system for high-throughput data acquisition and semi-automated image analysis by describing an experiment in which we acquired images of ~280000 particles of GroEL from a single grid in a continuous 25 h session at the microscope. In addition to characterizing the accuracy of Leginon's targeting, autofocus, and drift management routines, we have used ice thickness measurements to sort and select GroEL particles into 10 equivalent data sets each containing at least 220000 asymmetric units. The resolution of the reconstructed density maps resulting from these sorted datasets was used to assess the effect of ice thickness on the quality of the 3D volume. The ability to link the final reconstruction with the stored metadata related to the experiment provides a basis for assessing the limitations and bottlenecks of high-throughput macromolecular microscopy. We anticipate these methods will be applicable to a large number of specimens.

2. Materials and methods

Achieving high-throughput data acquisition requires both efficient data collection and a grid reasonably well covered by a layer of vitreous ice of suitable quantity and quality and containing specimen that is reasonably evenly distributed. Specimen grid preparation is thus an important aspect of this process and we include a discussion of these procedures here. We also address other aspects of the automated processing pipeline including particle selection, CTF estimation, and reconstruction procedures.

2.1. GroEL is used as a test specimen

GroEL was chosen as a test specimen for a number of reasons. It is a homo-tetradecamer that forms two back-to-back stacked heptameric rings with a molecular weight of about 840 kDa. The system has been extensively studied both structurally and functionally (Ludtke et al., 2004; Ranson et al., 2001; Sigler et al., 1998). It is relatively simple to purify and is stable for long periods of time at 4 °C. The molecular weight and stability of the complex make it ideally suited to structural analysis using single particle methods. The D7 symmetry of the molecule also means that a set of 10000 particles will contribute 140000 asymmetric subunits to a reconstructed density map. This allows us to split the total dataset into sorted subsets for comparisons and yet have the possibility for sub-nanometer resolution from reconstructions of each subset. High-resolution structures of GroEL derived from X-ray crystallographic methods (Braig et al., 1994, 1995) provide good comparisons for assessing the quality of the GroEL data set. GroEL is also of biological interest. It is a member of the Hsp60 class of proteins that aid in protein folding and is coded by an essential gene in *Escherichia coli* (Fayet et al., 1989) highlighting the importance of its function.

2.2. CryoEM specimen preparation

The GroEL proteins used in this study were provided by George Farr and Art Horwich. Prior to vitrification, the GroEL was diluted to 3.2 mg/ml in 100 mM Hepes, pH 7.5, 10 mM $Mg(OAc)_2$, 10 mM KOAc, and 2 mM DTT. The specimens were then preserved in a layer of vitreous ice suspended over a holey carbon substrate. The holey carbon films consist of a thin layer of pure carbon fenestrated by 2 μm holes spaced 4 μm apart and suspended over 400 mesh copper grids. The holey carbon films were developed in our lab and are now commercially available from Protochips Inc. under the name *Cflats*. Prior to freezing, grids were treated in a plasma cleaner (Fischione Instruments, Inc.) using 75% argon and 25% oxygen for 30 s and then blotted and plunge frozen using an FEI Vitrobot (FEI, Inc.), within 1 h of treatment. This protocol results in fairly consistent and reproducible vitreous ice for a wide variety of specimens and buffer conditions (Quispe et al., 2004). The method has the further advantage that it requires little expertise and a relative newcomer can produce useable grids simply by following the documented protocol.

For the current experiment, a volume of 4 μl of 4 μM GroEL was applied to the plasma-cleaned *Cflat* grids and the Vitrobot was used for freezing with settings of 100% humidity, 4 °C, and a blot time of 3.0 s.

2.3. Microscope and instrumentation

Data were acquired using a FEI Tecnai F20 Twin transmission electron microscope equipped with a Gatan Ultrascan 4k × 4k CCD camera. The microscope was operated at an accelerating voltage of 120 KeV and an extraction voltage of 3900 V. A Gatan 626 cryostage was used to maintain the specimen at a temperature of −178 °C within the microscope. For the data collection, the microscope was carefully aligned just before beginning the Leginon session. This step

is critical for the stability of the Leginon imaging parameters during data collection.

2.4. Automated data acquisition: Leginon MSI application

Leginon is freely available to academic and non-profit institutions and can be downloaded from http://nramm.scripps.edu/. Leginon was set up as described in Suloway et al. (2005). Briefly, the Leginon MSI application was used to control the microscope and CCD camera to acquire images and automatically identify targets at a variety of magnification scales. A montage of low-magnification images (120×) was acquired to visualize the entire usable area of the grid (Fig. 1A). Holes covered by a layer of ice of suitable thickness were identified in images acquired at a nominal magnification of 800× (Fig. 1B). The center of the holes was refined and targets were selected relative to this hole using images acquired at a magnification of 5000× (Fig. 1C). Drift was monitored and the defocus and astigmatism adjusted using a low dose focus target offset from the targeted hole (Fig. 1C, blue cross) at a magnification of 50000×. Finally focal pairs of images one nearer-to-focus (NTF) and one farther-from-focus (FFF), were acquired at each of the selected targets (Fig. 1C, green crosses) using a magnification of 50000× (Fig. 1D). Leginon controls the state of the microscope and camera using user-defined "preset" states of the microscope and CCD; these presets can be considered analogous to modes of the low dose kit on the microscope. For the experiment described here, seven presets were used as described in Table 1. Once Leginon was running stably, the only human intervention required during the experiment was to periodically replenish the cryogens in the cryo-stage dewar and the cold trap.

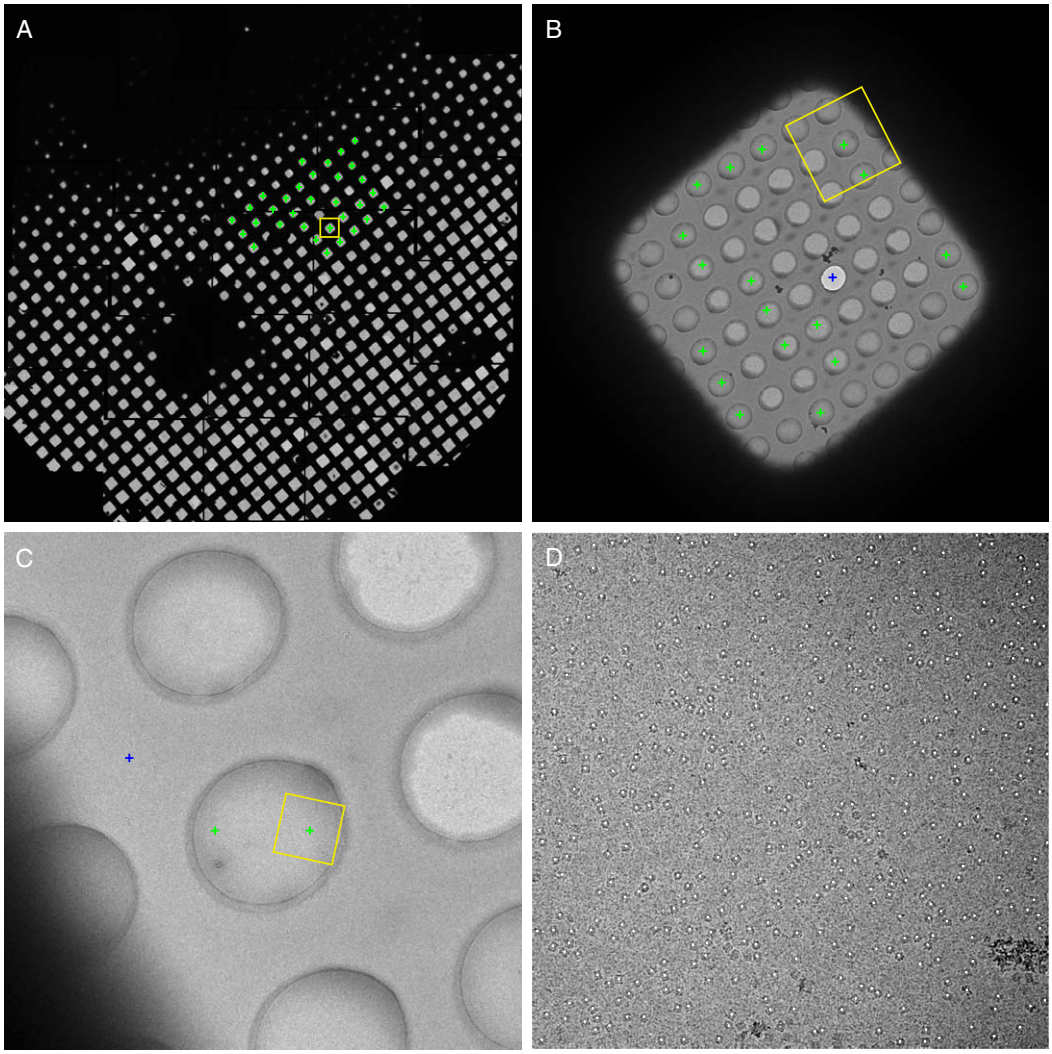

Fig. 1. Multiscale imaging with Leginon. (A) Montage of the *CFlat* grid showing squares that were targeted for further imaging (green crosses). The square shown in (B) is indicated by the yellow box. (B) An example image of a square. Holes that had ice thickness that fell within a user-specified range were targeted for further imaging (green crosses). The hole on which *z*-height correction was performed is indicated by the blue cross. The hole shown in (C) is indicated by the yellow box. (C) An example image of a hole. In each hole, two regions were targeted for high-resolution data acquisition (green crosses), as well as an area adjacent to the hole for focusing (blue cross). (D) An example high-resolution micrograph showing GroEL particles that were automatically identified using Selexon (white dots).

Table 1
Description of Leginon presets used for the acquisition of GroEL data

Preset name	Nominal magnification	Pixel size (nm/pixel)/field of view (μm)	Defocus (μm)	# of images recorded	Usage
gr	120	745/381	0	23	Acquiring images of the entire grid Targeting squares
sq	800	55.8/57.1	−2000	32	Acquiring images of squares Targeting holes
hl	5000	17.9/9.16	−150	318	Acquiring images of holes Targeting region of hole image for autofocus, and high-resolution exposures Autofocusing for eucentric-height correction
fa	50 000	0.905/0.927	−2.0		Acquiring images for autofocusing
fc	50 000	0.226/0.116	−2.0	273	Acquiring post-focus images
en	50 000	0.226/0.927	−0.8 to −2.0	552	Acquiring near-to-focus images
ef	50 000	0.226/0.927	−2.5	552	Acquiring far-from-focus images

2.5. Automated particle selection

Particles were selected from the CCD images using an automated particle selection software package called Selexon (Zhu et al., 2004). Selexon serves as a wrapper for the FindEM software (Roseman, 2003), interacting with the Leginon database and passing images to FindEM for picking. The FindEM algorithm uses a fast local cross-correlation search to find particles based on user-defined templates. For the GroEL data set, templates were defined by picking particles by hand from several FFF images. The handpicked particles were then aligned and classified and two class averages were selected, one of which represented particles primarily in top views, and one that represented particles in side views. These templates were used to automatically identify particles in the FFF images, as these images are acquired using high defocus and thus provide relatively higher contrast (Fig. 1D). The Selexon package provides utilities to calculate the shift and rotation between two images of a focal pair so that particles identified in the higher contrast further from focus images can be extracted from the nearer to focus images. Selexon also provides filters that identify areas of debris in the images and eliminates particle coordinates near these areas. In practice, Selexon can be started as soon as Leginon starts collecting data, and it will run continually, checking the database for new images, until data collection is completed and the process is stopped. The particle coordinates can be uploaded to the Leginon database and viewed using standard web browsers.

2.6. CTF estimation and correction

During the acquisition of images using Leginon, autofocusing is performed for every hole in which high-resolution data will be acquired, and this occurs at a position on the carbon adjacent to the hole (Fig. 1C, blue cross). An image is acquired from this position using a fixed defocus value. The defocus is then set to the value requested for the NTF image and the first high-magnification image is acquired at the selected target (Fig. 1C, green crosses). The defocus is then reset to the requested FFF value and the FFF image is acquired. Thus the NTF images can in theory be corrected based on the defocus estimated from either (i) the images acquired over the carbon at the low dose focus position or, (ii) the FFF image acquired at the relatively high defocus value, or (iii) the NTF image itself. The defocus estimates provided by the first two options are potentially more reliable due to the higher contrast of these images, but, as we will discuss below, the focus offsets applied are not necessarily predictable.

The Automated Contrast Transfer Function (CTF) Estimation (ACE) program (Mallick et al., 2005) was used to estimate the defocus of images acquired over the carbon at the low dose focus position as well as the defocus for each of the images of the final high-magnification focal pair (ACE is freely available and can be downloaded from http://nramm.scripps.edu/). The ACE program interacts directly with the Leginon database and is launched from a simple user interface developed under the MATLAB (The Mathworks, Inc.) programming environment. The estimated defocus values and other parameters associated with the CTF fit are automatically stored back to the Leginon database. ACE also calculates a confidence value from 0.0 to 1.0 where 1.0 is a perfect match, and this value can be used to evaluate the quality of the fit. In practice, we commonly throw out any micrograph with an ACE confidence value less than 0.8. The ACE program additionally provides utilities for using the estimated defocus to apply the appropriate phase reversals in Fourier space to the images prior to extracting the particles. ACE required ~1.5 min/micrograph to estimate the CTF for the 4096×4096 pixel images.

The ACE program was recently extended to allow for the estimation of the CTF parameters using an image formed from the incoherent sum of a stack of selected particles rather than the entire micrograph. This new module, called ACEMAN, reads in a stack of particles (in IMAGIC format) and estimates the defocus, envelope, and noise components of the CTF using the EMAN formulation (Ludtke et al., 1999). ACEMAN then writes a new stack with the appropriate EMAN CTF information in the header. Stacks with the CTF estimated in this manner were used for the EMAN reconstructions for which we performed full CTF correction.

2.7. Single particle reconstructions

Particles were selected from the phase-flipped NTF images and sorted by ice thickness into 10 sets containing the same number of particles (15839) and similar defocus ranges (see further discussion below). Three-dimensional electron density maps were then reconstructed from these sets of particles using the EMAN package (Ludtke et al., 1999). The initial model used in the refinements was from a previous reconstruction of GroEL that had been low pass filtered to 30 Å (data not shown). Several protocols were used for the reconstruction refinements. In protocol #1, the sets of particles were refined for four iterations using an angular increment of 4.5° and 8 rounds of iterative class averaging. The sets were then refined for four iterations using an angular increment of 4.5° with no iterative class averaging and using subpixel alignment. Finally, the sets were refined for four more iterations with an angular increment of 3.5°, no iterative class averaging, and subpixel alignment. Amplitudes were not corrected during the refinement in this first protocol. For refinement protocol #2, only the set of particles that had the thinnest ice were used. While the same particles were used, the stack was modified to have full CTF information in the header as described in the *CTF estimation and correction* section. The first eight iterations of the refinement were the same as in the first protocol. This was followed by six more iterations using an angular increment of 3.5°, no iterative class averaging, and subpixel alignment as before. However during these last six iterations, full ctf correction and automasking were applied (Ludtke et al., 2004). Finally in refinement protocol #3, the particles from all the sets were combined for a total of 158390 particles. This set of particles was refined for three iterations each with eight rounds of iterative class averaging. The refinement was then continued with no iterative class averaging and with subpixel alignment for eight more rounds at which time the refinement converged. The angular increment was 2° for all iterations in protocol #3. For all of the reconstructions approximately 76% of the total number of particles contributed to the final map.

For refinement protocols #1 and #3, the Spider software package (Frank et al., 1996) was used to correct the Fourier amplitudes for the final volumes by multiplying the maps by the square root of the ratio of the one-dimensional power spectrum of the EM map and the X-ray scattering curve for GroEL (http://ncmi.bcm.tmc.edu/eman/groel.sm) then low pass filtering the volumes to the appropriate resolution (Gabashvili et al., 2000).

The highest resolution reconstruction (7.8 Å) was deposited in the EM Database: Accession #1200.

2.8. Fitting of atomic structures into EM density

The Yammp molecular modeling package (Tan and Harvey, 1993) was used to fit the atomic structure of GroEL (PDB ID: 1OEL (Braig et al., 1995)) into the EM density maps. The GroEL atomic coordinates were reduced to only α-carbons, and the EM map was converted such that if an atom was inside a voxel, it was given a favorable energy score. The reduced GroEL structure was optimized in the EM volume using a Monte Carlo algorithm with simulated annealing such that the energy term was minimized.

3. Results

Data were collected during a 26-h session at the microscope during which data collection was primarily monitored by two people. Aligning the microscope, loading the grid into the cryostage, and initial Leginon calibrations and setup took approximately 1 h. Automated data collection then continued for 25 h during which time 552 high-magnification (50000×) defocus pairs were collected from 23 grid squares on which 318 holes were targeted (Table 1). Example targets for grid squares, holes, focus locations and high-resolution exposure locations are shown in Fig. 1. In total, automated data acquisition accounts for ~18 h of the 25 h Leginon session (Table 2). Of the remaining 7 h, ~1 h was lost because Leginon ran out of targets without the user realizing it, ~1 h was spent optimizing the Leginon calibrations, ~1 h was lost because Leginon's hole finder was initially poorly calibrated and this went unnoticed, and ~4 h were lost because the user was unable to complete the Leginon setup before another commitment and only resumed after 4 h had passed.

3.1. Specimen substrate and throughput

The choice of holey carbon films has proved to be a critical aspect in achieving high-throughput data acquisition. We had previously used Quantifoil holey carbon films (Quantifoil Micro Tools GmbH) with the same geometry as the *Cflats* used here. However, one problem that we experienced using these substrates was that we invariably observed an uneven distribution of ice across each hole. The ice around the circumference of the hole appeared considerably thicker than at the middle of the hole, presumably arising as a result of a lip around the edge of the hole. This non-uniform distribution of ice in turn resulted in a non-uniform distribution of the specimen; often, all of the particles were confined to the narrow layer of thick ice at the edge of the hole. Images acquired from these areas showed particles crowded too closely together and distributed over only a narrow band of the CCD frame. Although several data acquisition sessions

Table 2
Automated data acquisition timings

Activity	Total time spent
Atlas acquisition	4 min of acquisition + 30 min lens equilibration[a]
Square image acquisition and z-height adjustment	54 min
Focusing and drift monitoring	6.8 h
Focal pairs acquisition	9.4 h

[a] Since the objective lenses are turned off at 120× magnification, they must be turned back on and allowed to equilibrate before data acquisition could continue.

from samples prepared using these grids resulted in datasets containing more than 100 000 particles, the uneven particle distribution is what prompted us to explore alternative holey substrates. The new *Cflat* grids used for this experiment have a smaller lip at the edge of the hole than the Quantifoils and as a result the specimen is distributed fairly evenly across the entire hole (Fig. 1D).

3.2. Environmental conditions

The environmental conditions of the microscope room were monitored during the course of the experiment. The temperature of the ambient air, the chilled water entering and exiting the microscope, and the temperature a few inches inside of the exterior of the column were automatically recorded to the database every 4 min. An automated alert was sent to the operator if the temperatures strayed outside of set boundaries (Fellmann et al., 2006). These data can also be monitored visually from a web-based viewer both during and after the experimental session to verify the stability of the instrument during data acquisition. The data revealed no environmental anomalies during the course of this experiment.

3.3. Targeting accuracy

Accurate targeting across magnification scales of several orders of magnitude for extended periods of time is dependent on a good calibration of the goniometer (Pulokas et al., 1999; Suloway et al., 2005) and stable setup of the magnification presets. We calculated the targeting accuracy for squares (imaged at 800×) targeted at the grid level (120×), and holes (imaged at 5000×) targeted at the square level (800×). For this analysis, an acquired image (the child image) resulting from selecting a target on a lower magnification image (parent image) was compared to the region on the parent image that was expected to be captured in the child image. The distance of the center of the child image from the expected target on the parent is the measured error in targeting. The mean error for targeting squares for this experiment was 1.6 ± 0.3 μm, a fairly negligible offset when compared to the diameter of the entire square (~40 μm). The mean error for targeting holes was 0.84 ± 0.31 μm, a much larger relative error compared to the size of the holes (2 μm diameter). However this level of accuracy was adequate in ensuring that the targeted hole was the hole closest to the center of the acquired child image 99.4% of the time.

3.4. Ice thickness estimation

Ice thickness was estimated for every hole identified in every square (Fig. 2A). The estimate is based on an algorithm that determines the mean absorbance of a circular area at the center of each identified hole (Suloway et al., 2005). Holes were targeted for higher magnification exposures if they had an absorbance between 0.08 and 0.25 (Fig. 2A arrows). For the targeted holes, the ice thickness was measured again using an image of the hole acquired at a magnification of 5000× and these measurements fell into a range from 0.06 to 0.50 (Fig. 2B). The larger absorbance range measured for the holes reflects the fact that occasionally an incorrect hole was targeted. Some estimate of the thickness of the ice can also be measured from the high-magnification exposures by calculating the mean intensity at the center of the exposure image. Although it is difficult to convert the image absorbance to an absolute measure of ice thickness (see further discussion below), confidence in the relative measurements is provided by the fact that the absorbance measures correlate well across the three magnification scales (i.e. 800×, 5000×, and 50 000×). We were thus able to use the absorbance measures as a means of sorting particles into groups based on relative ice thickness.

3.5. Focusing accuracy and CTF estimation

Accurate focusing by Leginon is critical for high-quality data acquisition. As a part of Leginon's auto-focus routine, it acquires a post-focus image for which the CTF can be estimated to evaluate the accuracy of the focusing.

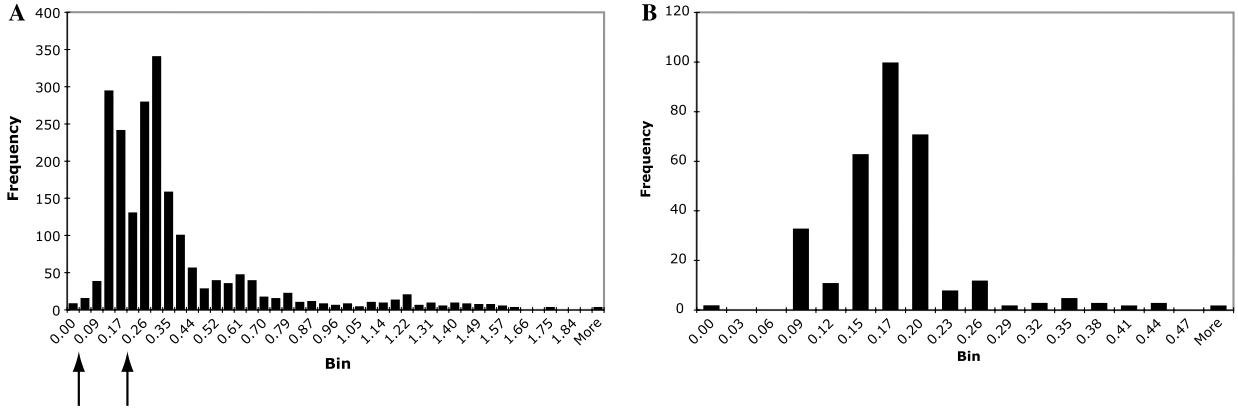

Fig. 2. Ice thickness analysis. (A) Distribution of ice thickness for all holes identified in all squares. Holes were targeted for higher magnification exposures if they had absorbance values between 0.08 and 0.25 (arrows). (B) Distribution of ice thickness values for all holes identified at the hl preset.

We used ACE to estimate the defocus for all of the post-focus images. Due to the relatively high signal-to-noise ratio for these images, ACE estimated the defocus very accurately with an average confidence value of 0.95 (see Section 2). When we compared the target defocus from Leginon to the estimated defocus from ACE, we found that the average focusing error was 34 nm with a standard deviation of 59 nm. This indicates that Leginon's auto focus routine is accurate enough to ensure that the defocus setting on the microscope is close to the desired setting of the user. Thus, the user can set Leginon to acquire data with a defined range of defoci such that the data covers the full spectrum of resolution with no gaps due to CTF zeros.

Accurate CTF estimation is crucial to achieving a high-resolution 3D reconstruction. As mentioned in the Section 2, correction of the CTF can be based on the defocus estimated from either: (i) the post-focus images acquired over the carbon at the low dose position; (ii) the FFF image acquired at the high-magnification target; or (iii) the NTF image acquired as the first of the focal pair and which is normally the only image that contributes particles to the final 3D map. Each of these estimates has advantages and disadvantages. The post-focus image has the highest signal-to-noise level due to the higher dose used in acquiring this image and the strong signal contributed by the carbon. However, this estimate might be inaccurate for the particles used in the reconstruction since the particle images are acquired in a neighboring area of the grid (the hole) that could be at a different relative height. The FFF image will have the same relative height as the NTF image and has the advantage of a higher dose, and greater relative defocus than the NTF image. However, since the FFF image is taken over a hole, the accuracy of the estimate of the CTF fit depends to a large extent on how many particles are present in the image. A potential disadvantage of estimating the CTF from either the post-focus or the FFF image is that the NTF image is normally acquired at a different defocus from either of these images. Thus, the accuracy of the CTF parameters used to correct the NTF images will depend on the accuracy with which this defocus offset can be applied at the microscope. While the defocus measured directly from the NTF images would in principal provide the most reliable estimate, in practice, the low dose used to acquire these images and the small amount of protein that contributes to the CTF curve, can cause the automated CTF estimation to fail.

Because of these issues, we have used the large dataset acquired for this experiment to systematically investigate the errors incurred in each of these estimation methods. Using Leginon, the nominal defocus for every acquired image is stored to the database. The defocus values estimated by ACE for the post-focus images are very accurate. We can thus use these values to calculate the offset between the nominal (the defocus Leginon attempted to achieve) and actual defocus settings for the focus images and thus determine the expected defocus for the NTF and FFF images. Since we also used ACE to estimate the defocus directly from the NTF and FFF images, we can calculate the difference between the expected defocus and the estimated ACE defocus to evaluate how close is the actual defocus to the target defocus. One would expect that since the focus position is slightly displaced from the NTF and FFF positions, there will be a slight change in the height of the grid between the two positions and thus an offset between the expected and the measured defocus. This displacement should be consistent between the NTF and FFF images. Indeed, a plot of the offset for the NTF images vs. the offset for the FFF mages shows that the two values are correlated (Fig. 3A) indicating that the offset between the expected and measured values are consistent between the NTF and FFF images. However, the mean offset for the FFF images (-98 ± 15 nm) is different than the mean offset in the NTF images (-15 ± 15 nm). To determine the source of this difference, we examined the dependence of the measured offsets on the size of the change in the defocus between the FFF and NTF settings. If the microscope controls for setting the defocus were

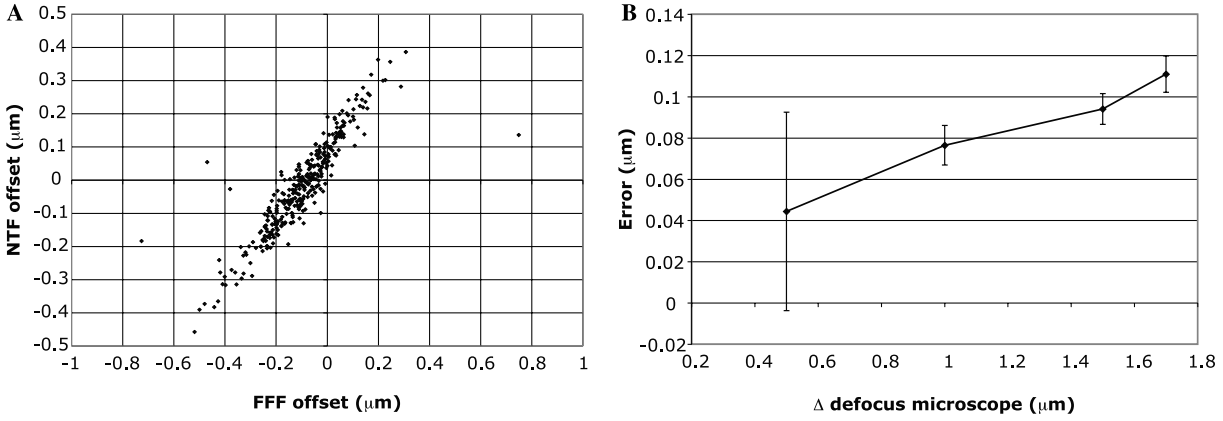

Fig. 3. Focus analysis. (A) The difference between the expected defocus and the measured defocus for the NTF images is plotted against that difference for the FFF images. While the values are correlated, the NTF values center around −15 nm and the FFF values center around −98 nm. (B) The measured change in the defocus between the FFF and NTF images is plotted against the expected change. This shows that the error for changing the defocus on the microscope is greater with greater defocus changes.

perfect, the measured change in the defocus between the FFF and NTF images should be the same as the expected change no matter how large the difference. Our results, however, indicated that the accuracy for setting the defocus on the microscope gets worse with greater defocus changes (Fig. 3B). Thus, if we were estimating the NTF defocus based on the FFF, we could be off as much as 170 nm for the nearest to focus images. As a result, we used the defocus measured directly from the NTF images to correct the CTF for the reconstructions presented in this paper, accepting only images for which the ACE confidence value was more than 0.8.

3.6. Specimen drift

The drift of the specimen was measured prior to taking the defocus pairs of high-magnification exposures. If a measured drift rate above 12 Å/s (value set by the operator) was observed, control of the microscope was passed to the Drift Manager node in Leginon. This node is responsible for monitoring the drift until it returns to a range where high-resolution imaging becomes possible (<12 Å/s), and also for recalculating targets if it is estimated that they will have shifted substantially as a result of a long and sustained period of specimen drift. The cryostage was quite stable during the collection of the GroEL data and the Drift Manager was only called on to intervene three times in the 25 h session. We have also calculated the drift rate over the course of the experiment by measuring the shift between the defocus pairs as shown in Fig. 4. Overlaid on this plot are the times when the cryostage was filled. The plot shows that, as expected, the drift rate spikes when liquid nitrogen is added to the stage and then settles over the course of ~12 min. The average drift rate during the experiment was 2.6 ± 0.8 Å/s. Since we used an exposure time for the high-resolution images of 0.1 s, this corresponds to an average specimen movement of ~0.3 Å during the time required to acquire the image.

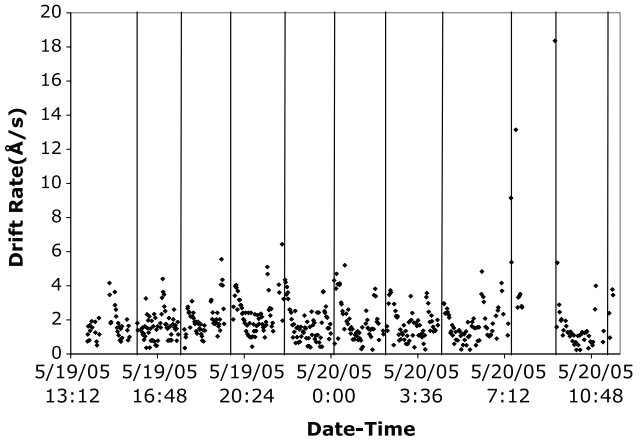

Fig. 4. Drift analysis. Drift rate measured from the defocus pairs plotted over time. The drift rate spiked whenever liquid nitrogen was added to the cryostage (vertical lines) and settles in ~12 min.

3.7. Particle selection

Particle images were automatically selected from the FFF images using the Selexon software. Two reference images were used as templates in the localized cross-correlation algorithm implemented in Selexon and resulted in 284 742 particles identified in the FFF images. The selected particles were then boxed out of the NTF images based on the coordinates identified in the FFF and compensating for any displacement measured using cross-correlation between the defocus pairs. Some particles identified in the FFF images were outside of the NTF images resulting in a final particle count of 283 325. The entire set of procedures for Selexon took ~3.75 min per defocus pair.

3.8. Single particle reconstructions

The size of the dataset acquired in this single experiment in combination with the high symmetry (D7) of the GroEL single particle allowed us to split the dataset into multiple subsets each containing sufficient numbers of asymmetric subunits to allow for sub-nanometer resolution in the reconstructed density map. This provided us with an excellent opportunity to mine the dataset in order to assess factors that influence the final resolution of the 3D map. One of these factors is almost certainly the thickness of the ice in which the sample is embedded. While it might seem more obvious that thin ice would be an advantage, the opposite argument has also been advanced on the grounds that thicker ice would provide a more stable substrate leading to higher resolution data.

We used the ice thickness measurements described above to sort the dataset into 10 subsets of particles with increasing ice thickness. To make meaningful comparisons of the 3D maps resulting from these sets, it is critical that each subset contain particles distributed over the same range of defocus values. To achieve this distribution, the particles were first sorted into three defocus groups based on the ACE measurements corresponding to small (−0.5 to −1.0 μm), medium (−1.0 to −1.5 μm), and large (−1.5 to −3.0 μm) defocus. Each of the micrographs in the defocus groups was then sorted by ice thickness into 10 subsets with equal numbers of micrographs and where each subset had increasing average ice thickness. The defocus groups were then recombined such that there were 10 subsets of particles ordered by ice thickness where each contained particles with small, medium, and large defocus values. Finally, particles were randomly removed from each subset to adjust the number of particles to that of the smallest subset, which contained 15 839 particles. In the end, we had generated 10 sets of 15 839 particles with equivalent ranges of defocus and with increasing average ice thickness.

Using the EMAN package and protocol #1 as described in the Section 2 (no amplitude correction during refinement), 3D density maps were calculated for each of the 10 subsets. The resolution was calculated for each reconstruction using the $FSC_{0.5}$ criterion. A plot of resolution vs. ice

thickness (Fig. 5) shows a trend in which the resolution of the reconstructed 3D map improved as the ice gets thinner. While the size of the overall difference in resolution between the maps derived from the thinnest and thickest ice is small, we note that we applied stringent control over the ice thickness of the holes from which data were acquired, thus the ice thickness varies only by a factor of two over the entire range.

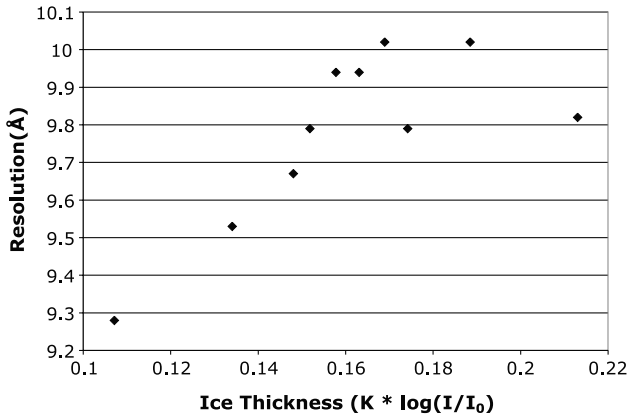

Fig. 5. Resolution of 10 separate GroEL reconstructions from particles sorted by ice thickness. The trend shows that the resolution of the reconstructions decreases with increasing ice thickness.

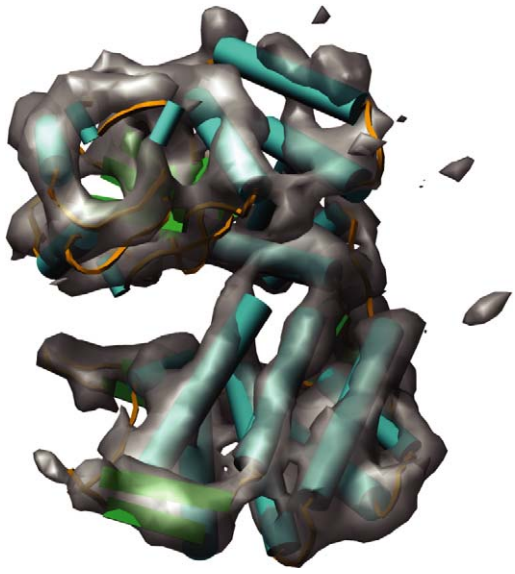

Fig. 7. Individual subunit of GroEL at 7.8 Å resolution. Tubes of density (gray) that correspond to α-helices of a crystal structure of GroEL (blue cylinders) are clearly visible.

The subset selected from the thinnest ice resulted in a reconstruction at a resolution of 9.3 Å and a surface rendering of the map is shown in Fig. 6A. At this resolution one

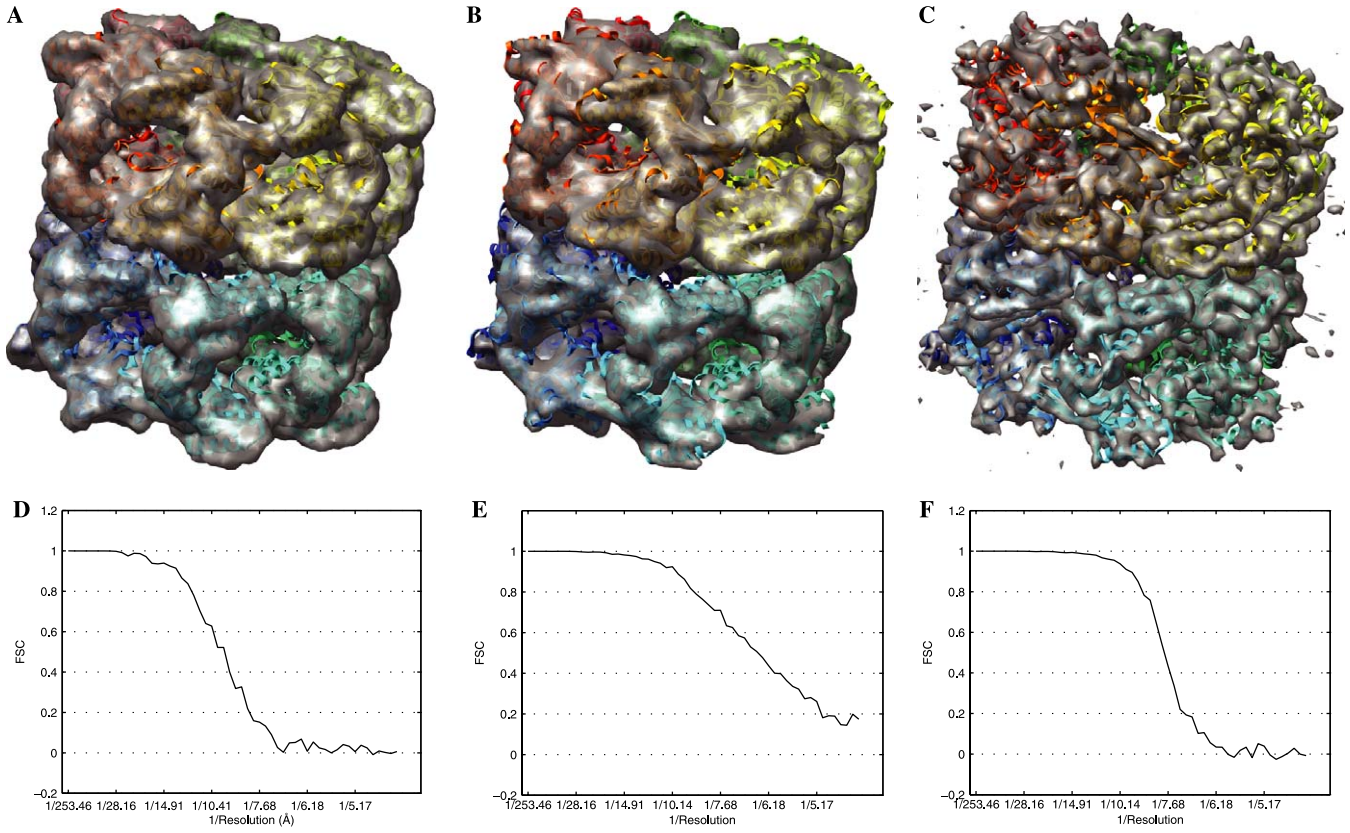

Fig. 6. GroEL reconstructed in three different ways. All volumes (A–C, gray) are shown in the same orientation with a crystal structure of GroEL (ribbons) fit into the density. (A) 9.2 Å resolution reconstruction of GroEL from 15 839 particles in the thinnest ice. The volume was amplitude corrected after the refinement. (B) 6.5 Å resolution reconstruction from the same particles as A. CTF amplitudes were corrected during the refinement. (C) 7.8 Å resolution reconstruction of GroEL from 158 390 particles. The volume was amplitude corrected after refinement. (D–F) FSC curves for (A–C), respectively. The FSC curve in E shows evidence of noise-bias.

can begin to make out cylinders that represent α-helices. This was verified by fitting a crystal structure of GroEL into the map using the Yammp package (Tan and Harvey, 1993). α-Helices in the crystal structure run through the center of the density of cylinders in the GroEL map.

The subset of particles with the thinnest ice was also reconstructed with full CTF correction during the refinement, i.e. Fourier amplitudes including the B-factor were corrected using EMAN for each iteration of the refinement (see protocol #2 in Section 2). This resulted in a reconstruction with a resolution of 6.5 Å (Fig. 6B). However, the 9.3 Å map and the 6.5 Å map have very similar features, and no new details were observable on the 6.5 Å map that were not also observable on the 9.3 Å map. This suggests that the resolution calculation is artificially skewed towards higher-resolution because of noise-bias, and this was made worse by the application of full CTF correction during the refinement (Stewart and Grigorieff, 2004).

Finally, we performed a reconstruction using particles from all of the 10 sets combined: 158 390 particles. For this reconstruction, no amplitude correction was applied during the refinement. This resulted in a reconstruction with 7.8 Å resolution. In contrast to the 6.5 Å map described above, this map had many additional details compared to the 9.3 Å map. The stack of helices in the equatorial domain of GroEL could be clearly identified in the 7.8 Å map (Fig. 7).

4. Discussion

We have demonstrated the potential for high-throughput data acquisition and analysis using Leginon, an automated system for low dose EM image acquisition. Images of more than a quarter of a million particles of GroEL were acquired in a single 25 h continuous session at the microscope. The only significant human intervention required was the periodic replenishment of liquid nitrogen in the cryostage and cold trap of the microscope. These data will be made publicly available at the NRAMM website (http://nramm.scripps.edu/). We have demonstrated the potential for an automated pipeline for molecular microscopy by showing that the data can be subjected to completely automated procedures to result in a three-dimensional (3D) reconstructed density map to better than 8 Å resolution. These automated procedures include particle selection and CTF determination, which are two of the most arduous and tedious steps required for single particle processing. Visual examination of the output of the automated particle selection (Selexon package) and the automated CTF determination (ACE package) confirm the satisfactory performance of these routines. Integration of the Selexon and ACE packages with the Leginon database greatly simplified the task of managing and manipulating the data and files. Together the Leginon, Selexon, and ACE packages provide a prototype for an automated pipeline where data are stored and managed using a relational database and a variety of web-based tools are used to examine and assess the outputs.

Analysis of the metadata acquired during the course of the experiment confirmed that the Leginon system and the microscope are very stable over a 25-h period of continuous data acquisition. The issue of specimen contamination has previously been raised (Zhang et al., 2001) as a potential limitation of the longevity of data collection from a vitreous ice specimen. However, we did not observe this to be a problem during the course of this experiment. We have also recently completed a series of systematic experiments to quantitate specimen contamination and found that this can be limited to less than 1 Å/h in the absence of film in the microscope (Cheng et al., in press).

Reconstructions of the GroEL particles separated into subsets sorted by ice thickness demonstrate the value of searching for the thinnest ice on the grid when acquiring data of the highest quality. It is difficult to establish the precise relationship between absolute ice thickness and absorbance (Cheng et al., in press), but we estimate that the ice thickness over the holes targeted in this data set ranged from ~150 to 300 Å. This means that the thinnest ice was only just thicker than the diameter of the GroEL particles themselves.

We have only just begun mining the metadata stored in the database. We show here that by sorting particles by ice thickness, we can separate higher-resolution data from lower-resolution data. This suggests that for any specimen we can "tune" the data collection and analysis such that we analyze the data from holes with only a narrow range of ice thickness that corresponds to the optimum thickness for that particular specimen. There may be other important parameters for achieving high-resolution such as selecting particles with the lowest drift rate, etc. Maintaining a relational database that logs these parameters makes it possible to quantitate how these parameters affect resolution.

Our reconstructions clearly demonstrate the danger of interpreting the resolution of a map where CTF amplitudes are corrected during the iterative refinement. We performed one reconstruction with no amplitude correction during the refinement and achieved 9.3 Å resolution. When we used exactly the same particles and applied amplitude correction during the refinement, the structure refined to 6.5 Å. The 6.5 Å map had little if any additional detail compared to the 9.3 Å map. The 6.5 Å reconstruction also had the problem that the FSC curve did not fall to zero at high frequencies. When we increased the number of particles by a factor of 10, and reconstructed them without amplitude correction during the refinement, the particles reconstructed to 7.8 Å. The 7.8 Å map had much more detail compared to the 9.3 and 6.5 Å maps with clearly defined tubes of density for the α-helices of GroEL. We conclude that although the 6.5 Å reconstruction is correct in that it has recognizable GroEL features, the resolution reported by the FSC curve is likely incorrect due to noise-bias that was amplified by performing CTF amplitude correction during the refinement (Stewart and Grigorieff, 2004).

We have shown that for well-behaved specimens like GroEL, it is possible to achieve sub-nanometer resolution

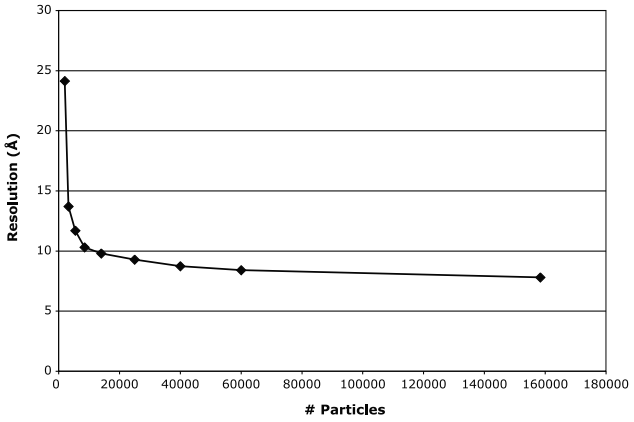

Fig. 8. Scatter plot of resolution as a function of the number of particles contributing to the refinement. Sets of increasing numbers of particles were randomly selected from the GroEL data set and were refined to convergence. The increase in resolution from the addition of particles tapers off at around 10 000 particles.

reconstructions from data acquired during a single session at the microscope. This was demonstrated both for a single subset of the particles selected from the thinnest ice (~16 000 particles, corresponding to ~224 000 asymmetric units) as well as for the complete dataset (160 000 particles, corresponding to ~2 240 000 asymmetric units). These numbers suggest that we can acquire sufficient data in 24 h to achieve sub-nanometer resolution from asymmetric macromolecules (e.g. ~250 000 particles), and also suggests the potential for using automated methods to extend the resolution of reconstructions still further if various technical hurdles can be addressed.

We believe that the resolution obtainable for reconstructions from this dataset is limited by the pixel size of the images (2.26 Å/pixel) rather than the number of particles contributing to the map. A graph of resolution vs. number of particles included in the refinement shows that the improvement in resolution gained by the addition of more particles tapers off very sharply at around 10 000 particles (Fig. 8). We hypothesize that this is most likely the point at which the refined map is of high enough quality to allow particles to be classified and aligned fairly accurately for each iteration so that the only effect of adding more particles is to gradually improve the signal-to-noise ratio. Several other reconstructions of GroEL have used far fewer particles to achieve higher or equivalent resolution reconstructions (Ludtke et al., 2004; Ranson et al., 2006). However, these reconstructions were obtained from data acquired to film, and the fewer particles required may possibly be attributed to film having better MTF characteristics than the CCD camera (Sander et al., 2005). Furthermore, the issue of the interpretation of the FSC curves makes it difficult to make quantitative comparisons without additional supporting experimental data.

Nevertheless, for data collected to a CCD camera, it is clear that improving the resolution will require higher magnification in order to decrease the pixel size and reduce the damping effect of the MTF for the high-resolution signal. Acquiring data at higher magnification will entail several challenges. If the pixel size were decreased from 2.26 Å/pixel to approximately 1 Å/pixel, then in order to acquire the same number of particles as the current data set, we would need to extend the length of the data acquisition experiment, improve the rate of data acquisition, or extend the area of the CCD camera by a factor of five. We are optimistic that some or all of these solutions will become feasible over the next several years and, when combined with the expected advances in computational power, will enable the acquisition and analysis of the millions of particles present on a single specimen grid and bring the possibility of single particle atomic resolution within reach.

Acknowledgments

The GroEL sample was kindly provided by George Farr and Art Horwich of Yale University and TSRI. The work presented here was conducted at the National Resource for Automated Molecular Microscopy which is supported by the National Institutes of Health though the National Center for Research Resources' P41 program (RR17573). Additional support was provided to S.M.S. through a fellowship from the NIH (GM073509-02).

References

Braig, K., Adams, P.D., Brunger, A.T., 1995. Conformational variability in the refined structure of the chaperonin GroEL at 2.8Å resolution. Nat. Struct. Biol. 2, 1083–1094.

Braig, K., Otwinowski, Z., Hegde, R., Boisvert, D.C., Joachimiak, A., Horwich, A.L., Sigler, P.B., 1994. The crystal structure of the bacterial chaperonin GroEL at 2.8 A. Nature 371, 578–586.

Carragher, B., Kisseberth, N., Kriegman, D., Milligan, R.A., Potter, C.S., Pulokas, J., Reilein, A., 2000. Leginon: an automated system for acquisition of images from vitreous ice specimens. J. Struct. Biol. 132, 33–45.

Cheng, A., Fellmann, D., Pulokas, J., Potter, C.S., Carragher, B., 2006. Does contamination buildup limit throughput for automated CryoEM? J. Struct. Biol. 154, 303–311.

Fayet, O., Ziegelhoffer, T., Georgopoulos, C., 1989. The groES and groEL heat shock gene products of *Escherichia coli* are essential for bacterial growth at all temperatures. J. Bacteriol. 171, 1379–1385.

Fellmann, D., Banez, R., Carragher, B., Potter, C.S., 2006. Temperature monitoring of an EM environment. Microsc. Today 14, 24–28.

Fellmann, D., Pulokas, J., Milligan, R.A., Carragher, B., Potter, C.S., 2002. A relational database for cryoEM: experience at one year and 50,000 images. J. Struct. Biol. 137, 273–282.

Frank, J., 2005. Three-Dimensional Electron Microscopy of Macromolecular Assemblies: Visualization of Biological Molecules in Their Native State. Oxford University Press, NewYork.

Frank, J., Radermacher, M., Penczek, P., Zhu, J., Li, Y., Ladjadj, M., Leith, A., 1996. SPIDER and WEB: processing and visualization of images in 3D electron microscopy and related fields. J. Struct. Biol. 116, 190–199.

Gabashvili, I.S., Agrawal, R.K., Spahn, C.M.T., Grassucci, R.A., Svergun, D.I., Frank, J., Penczek, P., 2000. Solution structure of the *E. coli* 70S ribosome at 11.5 Å resolution. Cell 100, 537–549.

Glaeser, R.M., 1999. Review: electron crystallography: present excitement, a nod to the past, anticipating the future. J. Struct. Biol. 128, 3–14.

Glaeser, R.M., 2004. Historical background: why is it important to improve automated particle selection methods? J. Struct. Biol. 145, 15–18.

Henderson, R., 1995. The potential and limitations of neutrons, electrons and X-rays for atomic resolution microscopy of unstained biological molecules. Q. Rev. Biophys. 28, 171–193.

Ludtke, S.J., Baldwin, P.R., Chiu, W., 1999. EMAN: semiautomated software for high-resolution single-particle reconstructions. J. Struct. Biol. 128, 82–97.

Ludtke, S.J., Chen, D.H., Song, J.L., Chuang, D.T., Chiu, W., 2004. Seeing GroEL at 6 A resolution by single particle electron cryomicroscopy. Structure (Camb.) 12, 1129–1136.

Mallick, S.P., Carragher, B., Potter, C.S., Kriegman, D.J., 2005. ACE: automated CTF estimation. Ultramicroscopy 104, 8–29.

Pulokas, J., Green, C., Kisseberth, N., Potter, C.S., Carragher, B., 1999. Improving the positional accuracy of the goniometer on the Philips CM series TEM. J. Struct. Biol. 128, 250–256.

Quispe, J., Banez, R., Carragher, B., Potter, C.S., 2004. Improving automation for Cryo-EM specimen preparation. Microsc. Microanal. 10, 1508–1509.

Ranson, N.A., Clare, D.K., Farr, G.W., Houldershaw, D., Horwich, A.L., Saibil, H.R., 2006. Allosteric signaling of ATP hydrolysis in GroEL-GroES complexes. Nat. Struct. Mol. Biol. 13, 147–152.

Ranson, N.A., Farr, G.W., Roseman, A.M., Gowen, B., Fenton, W.A., Horwich, A.L., Saibil, H.R., 2001. ATP-bound states of GroEL captured by cryo-electron microscopy. Cell 107, 869–879.

Roseman, A.M., 2003. Particle finding in electron micrographs using a fast local correlation algorithm. Ultramicroscopy 94, 225–236.

Sander, B., Golas, M.M., Stark, H., 2005. Advantages of CCD detectors for de novo three-dimensional structure determination in single-particle electron microscopy. J. Struct. Biol. 151, 92–105.

Sigler, P.B., Xu, Z., Rye, H.S., Burston, S.G., Fenton, W.A., Horwich, A.L., 1998. Structure and function in GroEL-mediated protein folding. Annu. Rev. Biochem. 67, 581–608.

Stewart, A., Grigorieff, N., 2004. Noise bias in the refinement of structures derived from single particles. Ultramicroscopy 102, 67–84.

Suloway, C., Pulokas, J., Fellmann, D., Cheng, A., Guerra, F., Quispe, J., Stagg, S., Potter, C.S., Carragher, B., 2005. Automated molecular microscopy: the new Leginon system. J. Struct. Biol. 151, 41–60.

Tan, R.K.-Z., Harvey, S.C., 1993. Yammp: Development of a Molecular Mechanics Program Using the Modular Programming Method. J. Comp. Chem. 14, 455–470.

Unwin, N., 2003. Structure and action of the nicotinic acetylcholine receptor explored by electron microscopy. FEBS Lett. 555, 91–95.

Zhang, P., Beatty, A., Milne, J.L., Subramaniam, S., 2001. Automated data collection with a Tecnai 12 electron microscope: applications for molecular imaging by cryomicroscopy. J. Struct. Biol. 135, 251–261.

Zhu, Y., Carragher, B., Potter, C.S., 2004. Contaminant detection: improving template matching based particle selection for cryo-electron microscopy. In: Proceedings of 2004 IEEE International Symposium on Biomedical Imaging, 1071–1074.